Native mass spectrometry reveals binding interactions of SARS-CoV-2 PLpro with inhibitors and cellular targets

Virginia K. James[1], Rianna N. Godula[2], Jessica M. Perez[2], Jamie P. Butalewicz[1], Sarah N. Sipe[1], Jon M. Huibregtse[2], Jennifer S. Brodbelt[1*]

[1]Department of Chemistry, The University of Texas at Austin, Austin, TX 78712

[2]Department of Molecular Biosciences, The University of Texas at Austin, Austin, TX 78712

Abstract

Here we used native mass spectrometry (native MS) to probe a SARS-CoV protease, PLpro, which plays critical roles in coronavirus disease by affecting viral protein production and antagonizing host antiviral responses. Ultraviolet photodissociation (UVPD) and variable temperature electrospray ionization (vT ESI) were used to localize binding sites of PLpro inhibitors and revealed the stabilizing effects of inhibitors on protein tertiary structure. We compared PLpro from SARS-CoV-1 and SARS-CoV-2 in terms of inhibitor and ISG15 interactions to discern possible differences in protease function. A PLpro mutant lacking a single cysteine was used to localize inhibitor binding, and thermodynamic measurements revealed that inhibitor PR-619 stabilized the folded PLpro structure. These results will inform further development of PLpro as a therapeutic target against SARS-CoV-2 and other emerging coronaviruses.

Introduction:

As part of the non-structural protein 3 (nsp3) protein of SARS-CoV-2,[1] PLpro is required for generation of nsp1-4 by proteolytic cleavage of the orf1a polyprotein. [2] PLpro is an approximately 36 kDa domain within the much larger nsp3 protein.[3] In addition to generation of the nsp1-4 proteins, SARS-CoV-2 PLpro modulates host responses by antagonizing the function of ISG15, an interferon-induced ubiquitin-like protein. It does this by catalyzing the cleavage of the isopeptide bond that links the C-terminus of ISG15 to the ε-amino group of lysine side chains of host and viral proteins.[2] Consistent with this dual role of PLpro, the cleavage sites within the orf1a polyprotein bear striking amino acid similarity to the C-terminus of ISG15. Thus, therapeutic inhibition of PLpro would be expected to both disrupt viral protein production and restore the anti-viral activities of ISG15.[4]

Given its importance in disease progression, several avenues for PLpro inhibition have been explored. The active site of PLpro (defined in part by C111, H272, and D286 of the PLpro only domain) may be occupied by small molecules that inhibit protease activity, and several molecules such as GRL-0617[5] and its derivatives[6] have been shown to bind and inhibit PLpro, with x-ray crystal structures of the complexes available in some cases. Structures with other inhibitors, including rac5c and rac3k[7] and several nanomolar-affinity 2-phenylthiophenes compounds, have also been determined.[8] Crystal structures of PLpro•peptide inhibitor complexes have also been solved[9], as well PLpro bound to ISG15[2] as well as ubiquitin and dimeric ubiquitin.[10] Other methods such as nuclear magnetic resonance (NMR) have been used for validation of crystal structures[11] as well as to track PLpro inhibitors that disrupt the interaction between PLpro and ISG15.[5] Biological assays including *in vitro* inhibition experiments have shown successful inhibition of PLpro by many small molecule inhibitors such as 6-thioguanine,[12] PR-619[13] and many others.[14–20] IC_{50} measurements based on monitoring cleavage of the nsp domain site or a polyubiquitin protein in the absence and presence of inhibitors have been widely used to evaluate numerous inhibitors[19,21–24] and nanobodies.[25] As PLpro is a zinc binding protein, it may also be inhibited allosterically by ejection of zinc thus causing protein misfolding,[26] and a recent study found that several small molecule inhibitors can eject zinc from PLpro.[27]

Mass spectrometry (MS) has also emerged as a powerful tool for analysis of proteases such as PLpro, affording accurate masses of cleavage peptides and intact proteins. Liquid chromatography mass spectrometry analysis of tryptic digests of PLpro (i.e., bottom-up proteomics) has shown utility in assays for detecting SARS-CoV-2 via identification of peptides from the virus in complex matrices such as blood and urine,[28] and this method has also localized covalently bound inhibitors to PLpro.[27,29] Crosslinking mass spectrometry revealed that interferon-induced ISG15 protein binds in a different region of PLpro compared to other ubiquitin and dimeric ubiquitin.[30] Analysis of intact, denatured PLpro (i.e. top-down proteomics) has been used to differentiate non-covalent and covalently bound inhibitors, especially when multiple inhibitors molecules are bound.[27] While these mass spectrometry techniques involving denatured proteins have been successful in characterizing covalently bound inhibitors, non-covalent interactions are not preserved under denaturing conditions and any information about protein tertiary structure is lost.

Native MS, which involves analyzing proteins in aqueous solutions of high ionic strength, is an attractive alternative as non-covalent interactions may be preserved as proteins are transported to the gas phase by electrospray ionization, allowing retention of protein conformations that resemble solution structures.[31–33] The scope of problems that native MS can solve has expanded with the emergence of other auxiliary methods, including collision induced unfolding (CIU) and collision cross section (CCS) measurements,[33,34] variable temperature electrospray ionization (vT-ESI),[35–37] and alternative MS/MS methods, such as ultraviolet photodissociation (UVPD).[38] vT-ESI allows determination of melting temperatures of proteins and protein complexes[36] and measurement of thermodynamic parameters associated with ligand binding.[37,39] UVPD has been used to localize inhibitor binding regions of proteins[40] and reveal unfolded/extended vs folded protein regions,[41] thus providing deeper insight into protein tertiary structure.

Native MS is well suited for examination of interactions between PLpro and inhibitors, particularly those that engage in non-covalent binding,[42] in addition to probing the interactions of PLpro and ISG15. Native MS has enabled the screening of many inhibitors to another SARS-CoV-2 protease, Mpro,[22,43–45] and to measure their effect on the thermodynamic parameters of Mpro.[39] Here we showcase the use of native MS to study interactions between PLpro, ISG15, and nsp domain cleavage sites and decipher the effects

that small molecule inhibitors have on PLpro activity and tertiary structure stability.

Methods:

Materials

Equine heart myoglobin, bovine ubiquitin, dithiothreitol, iodoacetamide, and ammonium acetate were purchased from Sigma-Aldrich (St. Louis, MO, USA). LC-MS grade water and methanol was purchased from Merck Millipore (Billerica, MA, USA). For experiments involving native-like charge states, proteins were diluted in a 100 mM ammonium acetate buffer to a final concentration of 10 µM and desalted with Micro Bio-Spin™ P-6 Gel Columns (Bio-Rad Laboratories Inc., Hercules, CA). For experiments with denaturing conditions, proteins were diluted in a denaturing 1:1 water–methanol solution containing 0.1% formic acid to a final concentration of 10 µM without further purification. Small molecule inhibitors were purchased from Cayman Chemicals and used as received. MS1 spectra, structures and masses are shown in **Figures S1-S2** and **Tables S1-S2,** and the MS/MS spectrum of PR-619 is shown in **Figure S3**. For inhibitor binding experiments, 100 µM of inhibitor was added to 10 µM of PLpro in 100 mM ammonium acetate and incubated for 30 minutes at room temperature.

Protein expression and purification

All proteins were generated in house as previously described, with some modifications.[12] The PLpro domain (residues 1-315) was defined as residues 1283 to 1597 of the SARS-CoV-2 ORF1a polyprotein which is equivalent to residues 746 to 1060 of nsp3. The PLpro domain of SARS-CoV-1 (residues 1-315) was defined as residues 1541-1855 of that SARS-CoV-1 ORF1a polyprotein, which is equivalent to residues 723 to 1037 of nsp3. All amino acid numbering that follows will be based on the isolated PLpro domains. SARs-CoV-2 PLpro WT and C111S mutant, PLpro from SARS-CoV-1, and Pro-ISG15-HA were purified as GST fusion proteins in BL21 *E. coli*. Overnight cultures were grown at 37 °C for all proteins. Cultures were diluted 1:20 and cultured with shaking for 2 hours at 37 °C. Expression of each protein was induced with 100 µM isopropyl β-D-1-thiogalactopyranoside (IPTG) overnight at 16 °C for all PLpro proteins and 3 hours at 30 °C for Pro-ISG15-HA. Cells were pelleted by centrifugation, resuspended in 10 mL PBS with 0.1% Triton X (Lysing Buffer), and sonicated for 1.5 minutes in 30 second intervals for lysing. Lysates were centrifuged at 10,000 x g for 10 minutes and supernatants were incubated with 100 µL of Glutathione Sepharose (GE Healthcare) and 1 mM phenylmethylsulfonyl (PMSF; Tocris) overnight with end-over-end rotation at 4 °C. Beads were washed three times with Lysis Buffer and three times subsequently with PC Buffer (50 mM Tris, 150 mM NaCl, 0.1% Triton X). Proteins were subjected to site-specific cleavage with PreScission Protease (GE Healthcare) to remove the GST tag. Beads were removed and the protein concentration in the supernatant was quantified by SDS-PAGE and Western blotting densitometry using a Licor Odyssey Imager. Protein sequences and monoisotopic masses are given in **Table S3**, and monoisotopic masses of expected PLpro1, PLpro2 and PLpro2 C111S complexes are summarized in **Table S4**. Sequence alignment of PLpro1, PLpro2 and PLpro2 C111S is shown in **Figure S4**, and MS1 spectra of native and denatured PLpro is shown in **Figure S5**.

Instrumentation

Most experiments were performed on a Thermo Scientific™ Q Exactive™ HF-X quadrupole-Orbitrap mass spectrometer (Bremen, Germany) with Biopharma option, which was modified to perform ultraviolet photodissociation (UVPD) in the HCD cell by addition of a 500 Hz 193 nm Coherent® ExciStar excimer laser (Santa Cruz, CA) as previously described.[46,47] A variable temperature ESI source was interfaced with the mass spectrometer as previously described, allowing extraction of thermodynamic parameters from van't Hoff plots created by monitoring the variations in the distribution of protein species as a function of solution temperature.[37,41] Experiments involving some of the solutions containing protein complexes were performed on a prototype Q Exactive Plus Ultra High Mass Range (UHMR) Orbitrap mass spectrometer (Thermo Fisher Scientific, Bremen, Germany), which was optimized for the preservation of weak, non-covalent interactions. Ions were generated by nano electrospray ionization using Au/Pd-coated borosilicate emitters fabricated in-house and using a spray voltage of 0.8-1.2 kV. The C-trap gas pressure was set to 0.5 to 1.0, corresponding to a UHV gauge reading of around 1E-10 to 1.5E-10 mbar, respectively. Throughout the course of this study, some variations in charge state distributions were observed for different solutions or when using the standard nanospray emitters versus the variable temperature source. Replicates of each category of experiment were collected on the same day to minimize these variations.

For MS1 and MS2 experiments, 7,500 and 240,000 resolution were used, respectively.

Tryptic digestion and LC-MS:

50 µg of apo PLpro2 was reduced with 5 mM dithiothreitol for 30 minutes at 55 °C and then alkylated with 15 mM iodoacetamide for 30 minutes at room temperature. The reduced and alkylated apo PLpro2 and 50 µg of unreduced apo PLpro2 were each individually digested with 1 µg of trypsin overnight at 37 °C. Both samples were desalted with C18 spin columns and analyzed using C18 chromatography on Dionex UltiMate 3000 high-performance liquid chromatograph (Thermo Fisher Scientific) coupled to a Thermo Fisher Scientific Orbitrap Fusion Lumos Tribrid mass spectrometer (San Jose, CA) with a data independent CID method as previously described.[48]

Data Acquisition and Processing

Variable temperature ESI data was analyzed using a custom MATLAB R2020a script as previously described.[41] UVPD mass spectra were deconvoluted using Xtract in QualBrowser, and sequence coverage maps and fragment abundance plots were generated from the deconvoluted data using MS-TAFI.[49] A custom version of MS-TAFI was used to compare UVPD replicate data so that only fragment ions identified in at least two out of three replicates were retained and 10 ppm error tolerance was used. Crystal structures were prepared using PyMol (PyMOL Molecular Graphics System, version 2.4 Schrödinger, LLC). CID_{50} values were determined by increasing the collisional activation voltage applied to disassemble a protein•inhibitor complex while monitoring the abundances of the apo protein and surviving protein•inhibitor complex. CID_{50} values were calculated in Origin(Pro), (2020b, OriginLab Corporation, Northampton, MA, USA.) using a Boltzmann sigmoidal function. LC-MS data was processed using Byonic.

Results and Discussion:

SARS-CoV-1 and SARS-CoV-2 PLpro display different affinities for cellular targets but not inhibitors

We used native MS to investigate the effects of inhibitors on PLpro and compare the outcomes for PLpro in SARS-CoV-1 (PLpro1) to SARS-CoV-2 (PLpro2). Under native conditions, all three variants of PLpro (PLpro1, PLpro2, and PLpro2 C111S) retained one zinc atom. PLpro1 has been shown to preferentially target ubiquitin chains, while PLpro2 targets the ubiquitin-like interferon-stimulated gene 15 protein (ISG15).[2] Both PLpro1 and PLpro2 bound monomeric ubiquitin with very low affinity (**Figures S6-S7**). Along with causing proteolysis of the interferon-induced ubiquitin-like precursor ProISG15 to ISG15 (**Figure S8**), PLpro2 also bound ISG15 with high affinity (**Figure S7**), whereas PLpro1 showed no binding to ISG15 (**Figure S6**). These results agree with prior reports that PLpro1 has lower affinity for ISG15 than does PLpro2[50] and that PLpro2 binds ISG15 with higher affinity than ubiquitin as ISG15 also interacts via a secondary site on PLpro2.[30] PLpro has 86% sequence conservation between SARS-CoV-1 and SARS-CoV-2 as shown in the sequence alignment in **Figure S4,** and while the catalytic site is conserved between the two viruses, differences emerge in the secondary binding site of ISG15 which accounts for its lower affinity for PLpro1.

The interaction of PLpro2 and ISG15 was localized by undertaking UVPD of the PLpro2●ISG15 complex, a method which has previously been show to map protein-ligand interactions based on variations in the abundances of fragment ions produced by apo versus holo proteins.[40] In essence, ligand binding results in formation of non-covalent interactions not present for the apo protein, typically leading to suppression of fragmentation of regions involved in the new interactions of the holo protein. Non-covalent interactions are preserved upon UVPD of the holo protein, preventing separation and release of fragment ions even if individual backbone bonds are cleaved. UVPD of the PLpro2●ISG15 complex (14+) resulted in an array of PLpro2 sequence ions as well as ejection of ISG15 (**Figure S9a**). There is a broad decrease in abundances of sequence ions corresponding to backbone cleavages near the N- and C- termini of PLpro2 upon UVPD of PLpro2●ISG15 relative to apo PLpro2 (**Figure S9b-d**). As the active site residues reside near both the N (C111) and C termini (H272, D286), these results agree with the crystal structure of PLpro2●ISG15 (**Figure S9e**), in which ISG15 binds around the active site.

Although previous studies have extensively evaluated interactions of PLpro1 and PLpro2 with ubiquitin, ubiquitin-like proteins,[30,50] and various small molecule drug candidates,[5,17,21] few studies have compared binding of small molecules to both PLpro1 and PLpro2. We selected seven potential inhibitors and evaluated them for binding to PLpro2. Solutions containing PLpro2 and each of the small molecule ligands were screened by native MS, and four exhibited low or no binding to PLpro2 (**Figure S10**) and were thus

discarded from further analysis. Complexes between PLpro2 and three of the small molecules (GRL-0617, HY-17542, and PR-619) were detected as seen by mass shifts added to PLpro2 in the MS1 spectra (**Figure 1a-d, S11-S12**). These same small molecules also bound to PLpro1. Prior studies have reported no PLpro inhibition, lower IC_{50} values, and/or only partial inhibition for the low binding inhibitors (SJB2-043, YM-155, K777, Jun9-72-2) versus the high binding inhibitors (GRL-0617, HY-17542, PR-619) (**Tables S1-S2**).[5,13,21,51,52] The similarity in binding trends for PLpro1 and PLpro2 seems reasonable given that the catalytic \triad (C111, H272 and D286) of the active site of PLpro is conserved between the two viruses, and these small molecules are not expected to bind secondary sites on the protein.

Inhibitor binding strength is commonly evaluated via IC_{50} values, and we note a substantial degree of variability among reported IC_{50} values for PLpro inhibitors. For example, the reported IC_{50} values for PR-619 in inhibition of PLpro2 vary between 1.83 μM[13] to 6.1 μM[21], thus making it critical to use a single uniform assay for comparisons of PLpro inhibitors. Instead of measuring IC_{50} values, we measured CID_{50} values for each of the high binding inhibitors. As derived from energy-variable collisional activation, the CID_{50} value corresponds to the collision energy at which 50% of the PLpro•inhibitor complexes have dissociated, thus providing insight into the relative stabilities of the complexes in the gas phase.[53,54] Complexes containing GRL-0617 exhibited lower CID_{50} values than complexes containing HY-17542, suggesting that GRL-0917 is more weakly bound (**Figure 2**). The CID_{50} values for PLpro1•PR-619 and PLpro2•PR-619 were unmeasurable as PR-619 remained bound all voltages, characteristic of a covalent binding mode. The CID_{50} values were similar for complexes containing PLpro1 or PLpro2, indicating no significant difference based on the sequences and structures adopted by these two PLpro proteins.

Next, we aimed to evaluate the inhibitor binding location and binding mode to PLpro2. The binding site of the most commonly studied inhibitor, GRL-0617, has been localized near the active site of PLpro2 based on several previously solved crystal structures,[5] and HY-17542 is expected to bind PLpro in a manner similar to GRL-0617 owing to their nearly identical structures (**Table S1**). Both GRL-0617 and HY-17542 resulted in a mass shift equal to the mass of the ligand (**Figure 1b,c**) prominence of the PLpro2•ligand

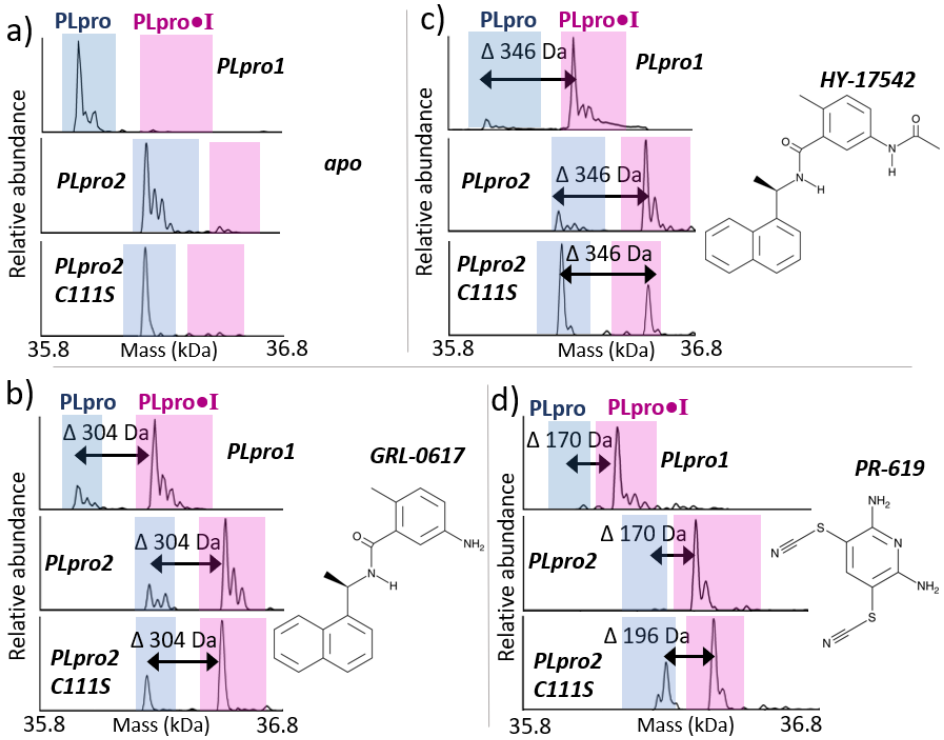

Figure 1. Deconvoluted mass spectra obtained for solutions containing 10 μM PLpro1, PLpro2, PLpro2 C111S (a) alone or with 100 μM inhibitor including (b) GRL-0617, (c) HY-17542, or (d) PR-619 in 100 mM ammonium acetate. In parts a-d, PLpro1, PLpro2, and PLpro2 C111S are shown in the upper, middle, and lower panels, respectively. Non-deconvoluted MS1 spectra are shown in **Figures S11-13**.

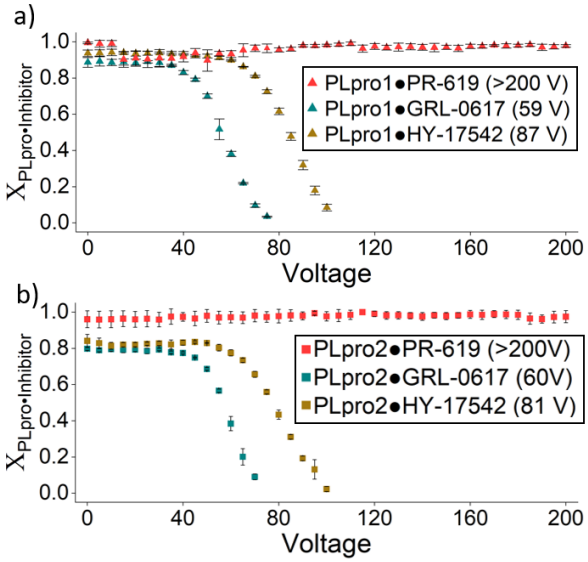

Figure 2. Energy-variable CID curves are shown for PLpro•inhibitor complexes containing PR-619, GRL-0617 or HY-17542 for (a) PLpro1 and (b) PLpro2. The derived CID_{50} values (±1 V) are summarized in the legend.

complexes relative to apo PLpro2 in the MS1 spectra. For PR-619, PLpro2 (and PLpro1) displayed a mass shift of 170 Da (**Figure 1d**) rather than the mass of the intact ligand (223 Da). PR-619 has a unique structural motif containing two thiocyanate groups. Collisional induced dissociation of PR-619 yields fragment ions corresponding to the loss of one or two cyano groups from the thiocyanate motifs, resulting in ions of *m/z* 196 and 170 (**Figure S3**). These results led us to postulate that PR-619 forms one or two disulfide bonds with one or two cysteine residues in PLpro2, in each case releasing one cyano group per new disulfide bond. Formation of two disulfide bonds with PLpro2 would correspond to a type of crosslinking.

While two previous studies evaluated interactions of PR-619 with PLpro2 and many others have used PR-619 for inhibition of related proteases, such as ubiquitin-specific proteases involved in cancer progression,[55,56] to our knowledge, no study has investigated the binding mechanism or location of PR-619 for deubiquitinating proteases. One important clue is obtained by examination of binding of PR-619 and the C111S mutant of PLpro2. This single point variant lacks the critical C111 in the active site triad, a site that is anticipated to be readily oxidized based on prior crystallographic evidence.[5] This C111S mutant alleviates the question of whether C111 is oxidized or reduced in PLpro2 and removes C111 as a binding site. PLpro2 C111S exhibits a mass shift equal to the mass of the inhibitor upon binding to GRL-0617 and HY-17542 (**Figure 1b-c, Figure S13**). The mass shift induced by PR-619 binding to PLpro2 C111S corresponds to 196 Da, not 170 Da as observed upon PR-619 binding to PLpro1 or PLpro2. The mass shift of 196 Da corresponds to the loss of a single cyano group from PR-619 (**Figure 1d, Figure S13**). Because PR-619 loses both cyano groups when binding to PLpro1 and PLpro2, we suspect that PR-619 forms disulfide bonds to two Cys (C111 and C146), both in close proximity (11 $Å^2$) in the crystal structure of PLpro (**Figure S14**). Zinc remains bound to all complexes, suggesting that the four cysteines (C189, C192, C224, C226) that are known to bind zinc are not involved in binding to PR-619. We attempted to confirm the PR-619 binding sites on PLpro using conventional bottom-up proteomics after tryptic digestion of PLpro•PR-619 without and with reduction/alkylation (the latter a common step in bottom-up proteolysis to enhance digestion efficiency). While we obtained coverage of the putative PR-619 binding sites (C111 and C146) after alkylation and reduction of PLpro2 (**Figure S15a**), no peptides that contained these two residues were detected without reduction and alkylation of PLpro2 (**Figure S15b**). Moreover, since PR-619 is expected to be coordinated to PLpro via two disulfides bonds, disulfide reduction should cleave the inhibitor and prevent its localization on the tryptic peptides. Given these impediments using a standard bottom-up approach, we focused on additional native MS experiments to confirm the binding location and mode of PR-619.

To further investigate the inhibitor binding modes, the survival of the complexes was examined by denaturing the solutions containing PLpro2 after incubation with each inhibitor for 30 minutes and then examining the resulting mass spectra (**Figures S16** and **S17**). As expected, both GRL-0617 and HY-17542 are dislodged in the denaturing solutions (**Figure S16**), consistent with their non-covalent binding interactions. Some PR-619 remains bound to PLpro2 in the denaturing solution, indicating it is covalently bound (**Figure S17**). The overall abundance of PLpro2•PR-619 to apo PLpro2 in **Figure S17** suggests that ~40% of the protein is unbound. As also seen in **Figure S17**, the ratio of PLpro2•PR-619 to apo PLpro2 decreases for the higher charge states for the denaturing solutions, indicating that strain from charge-induced protein elongation may further disrupt PR-619 binding despite the inhibitor being covalently bound.

The impact of the inhibitors on the interaction

of PLpro2 and ISG15 was also evaluated. Incubation of PLpro2 with ISG15 results in abundant PLpro2●ISG15 complexes (**Figure 3, Figure S18**). All three inhibitors disrupt binding of ISG15 when added to the solutions containing PLpro2 and ISG15 (**Figure 3**). Prior in vitro results have reported inhibition of SARS-CoV-2 in the presence of all three inhibitors including GRL-0617,[5,50] HY-17542,[20] and PR-619.[13,21] A previous NMR study also reported that GRL-0617 out-competed ISG15 to bind to PLpro2 when added to a solution containing PLpro2●ISG15.[5] Despite the differences in binding location and affinity, each inhibitor appears to disrupt binding of PLpro2 to ISG15.

Inhibitor PR-619 stabilizes PLpro tertiary structure.

To further probe the impact of inhibitor binding on PLpro2, UVPD was used to generate fragmentation patterns of apo PLpro2 and PLpro2• inhibitor complexes. UVPD has been used previously to reveal conformational variations in proteins, as fragmentation is generally enhanced in more flexible and less tightly organized regions. Ligand binding may also contribute to modulation of protein conformations because non-covalent interactions are re-organized during ligand binding. Networks of non-covalent interactions may suppress separation and release of fragment ions, an effect observed as a reduction in the abundances or number of fragment ions upon UVPD. The two non-covalent inhibitors, GRL-0617 and HY-17542, are released from PLpro2 during transfer to the collision cell, thus information about binding sites cannot be obtained by UVPD for complexes containing these weakly bound inhibitors. The UVPD mass spectra and sequence maps of PLpro2 and PLpro2•PR-619 are shown in **Figures S19-20**. The number of fragment ions that originate from cleavages PLpro2 and PLpro2•PR-619 without any supplemental collisional activation (0 V), suggesting similar structures. In-source collisional activation may be used prior to UVPD to induce protein unfolding,[57] and the variation in fragmentation observed upon UVPD of resulting fragmentation patterns can be monitored to reveal regions of the protein that are disrupted.[41] While of different backbone positions for PLpro2 and PLpro2•PR-619 were counted and plotted as a function of backbone position in **Figure 4**. There was little UVPD of PLpro2•PR-619 after no or low in-source collision activation resulted in insignificant differences in fragmentation compared to apo PLpro2, fragmentation increased for apo PLpro2 in the region spanning K105 to N144 after greater in-source collisional activation (200 V). This region of enhanced fragmentation of apo PLpro2 is demarcated on the sequence shown in **Figure 4b** and shaded on the crystal structure in **Figure 4c**. This region encompasses the suspected binding site of PLpro2•PR-619, suggesting that the suppression of UVPD fragmentation of PLpro2•PR-619 relative to apo PLpro2 indicates that PR-619 may stabilize the mid-section of PLpro. The loss of sequence coverage for PLpro2•PR-619 in the region between the C111 and the second suspected binding cite (C146) further supports C146 as the second PR-619 binding via a cross-linking mode that impedes fragmentation.

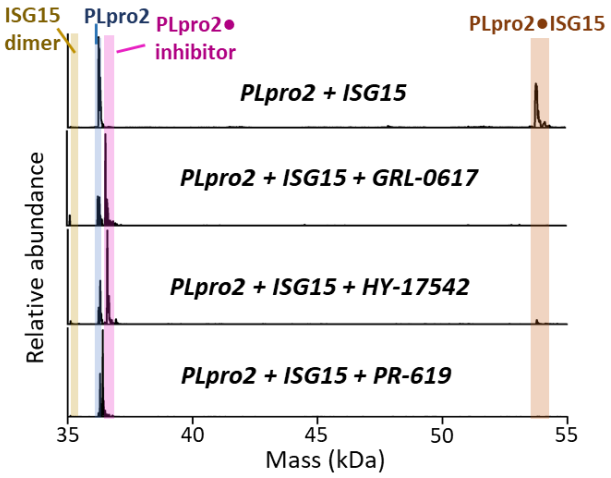

Figure 3. Deconvoluted mass spectra obtained for solutions containing both PLpro2 (10 µM) and ISG15 (10 µM) without or with each inhibitor (100 µM) in 100 mM ammonium acetate. Non-deconvoluted spectra are shown in **Figure S19**.

Variable temperature ESI (vT-ESI) analysis of apo PLpro2 and PLpro2•PR-619 was undertaken to evaluate variations in the thermodynamic parameters of PLpro2 upon PR-619 binding and probe any structural stabilization imparted by inhibitor binding. For this method, the charge state distributions of the protein are monitored as a function of the temperature of the solution (**Figure 5a**) and used to generate curves (**Figure 5b**) and van't Hoff plots (**Figure S21**) from which ΔG, ΔH, and ΔS are determined (**Figure 5c**). vT-ESI of apo PLpro2 shows that the protein retains zinc even at high temperatures, suggesting that zinc is strongly bound (**Figure 5a**). Zinc is only lost when the protein is sprayed from denaturing solutions (**Figure S16, 17**). The

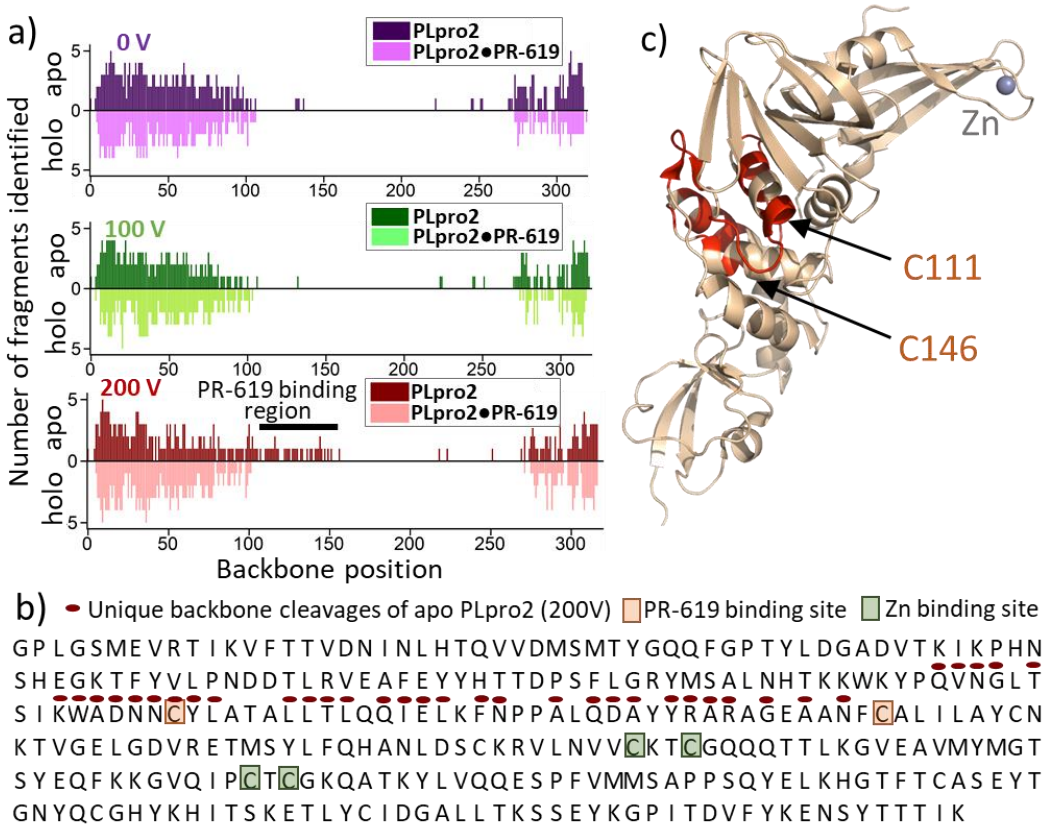

Figure 4. a) Mirror bar graphs showing the number of sequence ions originating from cleavages of each backbone position of apo PLpro2 (10+) and PLpro2●PR-619 (10+) upon UVPD (1 pulse, 2.5 mJ) when using 0, 100, or 200 V of in-source collisional activation. The light colored bars representing the fragmentation of PLpro2●PR-619 are shown below the dark bars for apo PLpro2, allowing better visualization of those regions for which fragmentation of PLpro2●PR-619 is suppressed relative to PLpro2. The backbone cleavage sites identified for apo PLpro2 that were not found for PLpro2●PR-619 are b) marked with red dashes above the residues on the sequence map and c) shaded in red on the crystal structure (PDB 6XA9), indicating regions where fragmentation is suppressed in the PLpro2●PR-619 complex.

vT-ESI data shows that apo PLpro2 shifts to high charge states as the temperature increases, consistent with protein elongation/unfolding which facilitate protonation of more basic sites. In contrast, PLpro●PR-619 shows less variation in its charge state distribution as a function of solution temperature, indicative of greater stability of the folded PLpro2●PR-619 complex (**Figure 5a,b**). Thermodynamic analysis of apo PLpro2 vs PLpro2●PR-619 reveals that unfolding of apo PLpro2 is entropically favorable (based on a positive trend in the entropy values), whereas unfolding of PLpro2●PR-619 is enthalpically favorable (based on a negative trend in the enthalpy values) (**Figures 5c, S21**). Enthalpic favorability of the thermal denaturation of PLpro2●PR-619 corresponds to an increase of intermolecular interactions which outweighs the restriction in entropy. These variable temperature ESI results affirm that PR-619 stabilizes the tertiary structure of PLpro2, which is congruent with a crosslinking binding mode.

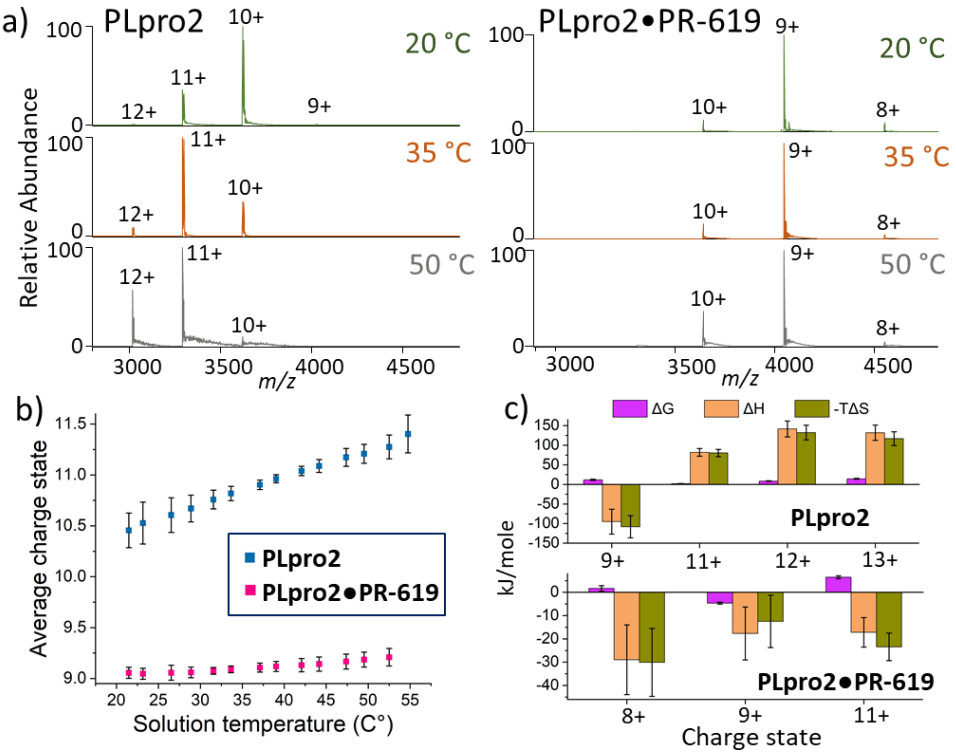

Figure 5. a) MS1 spectra of solutions containing PLpro2 (10 µM in 100 mM ammonium acetate) or PLpro2●PR-619 (10 µm protein and 100 µm ligand in 100 mM ammonium acetate) at 20, 35, and 50 °C, from which b) melting curves for apo PLpro2 and PLpro2●PR-619. c) From the melting curves, van't Hoff plots were determined (**Figure S21**) and used to calculate thermodynamic values. The 10+ charge state was used as the reference for both apo PLpro2 and PLpro2●PR-619.

Conclusions:

A comparison of PLpro from SARS-CoV-1 and SARS-CoV-2 was undertaken to evaluate the interaction of PLpro with inhibitors and ISG15. Using native MS, we confirmed that PLpro2 preferentially binds to ISG15 relative to PLpro1. At the same time, PLpro1 bound inhibitors designed for PLpro2. These results suggest that despite the differences in sequence conservation of PLpro between coronaviruses, the protease may still be a good therapeutic target for a broad range of coronaviruses.

We used ultraviolet photodissociation and a PLpro C111S mutant to localize the binding of PR-619, an inhibitor highlighted in several recent PLpro studies. We found that PR-619 acts as a crosslinker, stabilizing the tertiary structure of PLpro as supported by vT-ESI results. These results give insight into one of the binding mechanisms of PR-619, a widely used general inhibitor of deubiquitylating enzymes (DUBs).

Acknowledgments:

Funding from the National Institutes of Health (R35GM13965) and the Robert A. Welch Foundation (F-1155) to J.S.B. is gratefully acknowledged. This work was supported by a grant from the National Institutes for Allergy and Infectious Diseases (AI096090) to J.M.H.

References:

(1) Jahirul Islam, Md.; Nawal Islam, N.; Siddik Alom, Md.; Kabir, M.; Halim, M. A. A Review on Structural, Non-Structural, and Accessory Proteins of SARS-CoV-2: Highlighting Drug Target Sites. *Immunobiology* **2023**, *228* (1), 152302. https://doi.org/10.1016/j.imbio.2022.152302.

(2) Shin, D.; Mukherjee, R.; Grewe, D.; Bojkova, D.; Baek, K.; Bhattacharya, A.; Schulz, L.; Widera, M.; Mehdipour, A. R.; Tascher, G.; Geurink, P. P.; Wilhelm, A.; van der Heden van Noort, G. J.; Ovaa, H.; Müller, S.; Knobeloch, K.-P.;

Rajalingam, K.; Schulman, B. A.; Cinatl, J.; Hummer, G.; Ciesek, S.; Dikic, I. Papain-like Protease Regulates SARS-CoV-2 Viral Spread and Innate Immunity. *Nature* **2020**, *587* (7835), 657–662. https://doi.org/10.1038/s41586-020-2601-5.

(3) Amin, Sk. A.; Banerjee, S.; Ghosh, K.; Gayen, S.; Jha, T. Protease Targeted COVID-19 Drug Discovery and Its Challenges: Insight into Viral Main Protease (Mpro) and Papain-like Protease (PLpro) Inhibitors. *Bioorganic & Medicinal Chemistry* **2021**, *29*, 115860. https://doi.org/10.1016/j.bmc.2020.115860.

(4) Liu, G.; Lee, J.-H.; Parker, Z. M.; Acharya, D.; Chiang, J. J.; van Gent, M.; Riedl, W.; Davis-Gardner, M. E.; Wies, E.; Chiang, C.; Gack, M. U. ISG15-Dependent Activation of the Sensor MDA5 Is Antagonized by the SARS-CoV-2 Papain-like Protease to Evade Host Innate Immunity. *Nat Microbiol* **2021**, *6* (4), 467–478. https://doi.org/10.1038/s41564-021-00884-1.

(5) Fu, Z.; Huang, B.; Tang, J.; Liu, S.; Liu, M.; Ye, Y.; Liu, Z.; Xiong, Y.; Zhu, W.; Cao, D.; Li, J.; Niu, X.; Zhou, H.; Zhao, Y. J.; Zhang, G.; Huang, H. The Complex Structure of GRL0617 and SARS-CoV-2 PLpro Reveals a Hot Spot for Antiviral Drug Discovery. *Nat Commun* **2021**, *12* (1), 488. https://doi.org/10.1038/s41467-020-20718-8.

(6) Sanders, B. C.; Pokhrel, S.; Labbe, A. D.; Mathews, I. I.; Cooper, C. J.; Davidson, R. B.; Phillips, G.; Weiss, K. L.; Zhang, Q.; O'Neill, H.; Kaur, M.; Schmidt, J. G.; Reichard, W.; Surendranathan, S.; Parvathareddy, J.; Phillips, L.; Rainville, C.; Sterner, D. E.; Kumaran, D.; Andi, B.; Babnigg, G.; Moriarty, N. W.; Adams, P. D.; Joachimiak, A.; Hurst, B. L.; Kumar, S.; Butt, T. R.; Jonsson, C. B.; Ferrins, L.; Wakatsuki, S.; Galanie, S.; Head, M. S.; Parks, J. M. Potent and Selective Covalent Inhibition of the Papain-like Protease from SARS-CoV-2. *Nat Commun* **2023**, *14* (1), 1733. https://doi.org/10.1038/s41467-023-37254-w.

(7) Calleja, D. J.; Kuchel, N.; Lu, B. G. C.; Birkinshaw, R. W.; Klemm, T.; Doerflinger, M.; Cooney, J. P.; Mackiewicz, L.; Au, A. E.; Yap, Y. Q.; Blackmore, T. R.; Katneni, K.; Crighton, E.; Newman, J.; Jarman, K. E.; Call, M. J.; Lechtenberg, B. C.; Czabotar, P. E.; Pellegrini, M.; Charman, S. A.; Lowes, K. N.; Mitchell, J. P.; Nachbur, U.; Lessene, G.; Komander, D. Insights Into Drug Repurposing, as Well as Specificity and Compound Properties of Piperidine-Based SARS-CoV-2 PLpro Inhibitors. *Frontiers in Chemistry* **2022**, *10*.

(8) Shen, Z.; Ratia, K.; Cooper, L.; Kong, D.; Lee, H.; Kwon, Y.; Li, Y.; Alqarni, S.; Huang, F.; Dubrovskyi, O.; Rong, L.; Thatcher, G. R. J.; Xiong, R. Design of SARS-CoV-2 PLpro Inhibitors for COVID-19 Antiviral Therapy Leveraging Binding Cooperativity. *J. Med. Chem.* **2022**, *65* (4), 2940–2955. https://doi.org/10.1021/acs.jmedchem.1c01307.

(9) Rut, W.; Lv, Z.; Zmudzinski, M.; Patchett, S.; Nayak, D.; Snipas, S. J.; El Oualid, F.; Huang, T. T.; Bekes, M.; Drag, M.; Olsen, S. K. Activity Profiling and Crystal Structures of Inhibitor-Bound SARS-CoV-2 Papain-like Protease: A Framework for Anti–COVID-19 Drug Design. *Science Advances* **2020**, *6* (42), eabd4596. https://doi.org/10.1126/sciadv.abd4596.

(10) Vliet, V. J. E. van; Huynh, N.; Palà, J.; Patel, A.; Singer, A.; Slater, C.; Chung, J.; Huizen, M. van; Teyra, J.; Miersch, S.; Luu, G.-K.; Ye, W.; Sharma, N.; Ganaie, S. S.; Russell, R.; Chen, C.; Maynard, M.; Amarasinghe, G. K.; Mark, B. L.; Kikkert, M.; Sidhu, S. S. Ubiquitin Variants Potently Inhibit SARS-CoV-2 PLpro and Viral Replication via a Novel Site Distal to the Protease Active Site. *PLOS Pathogens* **2022**, *18* (12), e1011065. https://doi.org/10.1371/journal.ppat.1011065.

(11) Napolitano, V.; Dabrowska, A.; Schorpp, K.; Mourão, A.; Barreto-Duran, E.; Benedyk, M.; Botwina, P.; Brandner, S.; Bostock, M.; Chykunova, Y.; Czarna, A.; Dubin, G.; Fröhlich, T.; Hölscher, M.; Jedrysik, M.; Matsuda, A.; Owczarek, K.; Pachota, M.; Plettenburg, O.; Potempa, J.; Rothenaigner, I.; Schlauderer, F.; Slysz, K.; Szczepanski, A.; Greve-Isdahl Mohn, K.; Blomberg, B.; Sattler, M.; Hadian, K.; Popowicz, G. M.; Pyrc, K. Acriflavine, a Clinically Approved Drug, Inhibits SARS-CoV-2 and Other Betacoronaviruses. *Cell Chemical Biology* **2022**, *29* (5), 774-784.e8. https://doi.org/10.1016/j.chembiol.2021.11.006.

(12) Swaim, C. D.; Dwivedi, V.; Perng, Y.-C.; Zhao, X.; Canadeo, L. A.; Harastani, H. H.; Darling, T. L.; Boon, A. C. M.; Lenschow, D. J.; Kulkarni, V.; Huibregtse, J. M. 6-Thioguanine Blocks SARS-CoV-2 Replication by Inhibition of PLpro. *iScience* **2021**, *24* (10), 103213. https://doi.org/10.1016/j.isci.2021.103213.

(13) Große, M.; Setz, C.; Rauch, P.; Auth, J.; Morokutti-Kurz, M.; Temchura, V.; Schubert, U.

Inhibitors of Deubiquitinating Enzymes Interfere with the SARS-CoV-2 Papain-like Protease and Block Virus Replication In Vitro. *Viruses* **2022**, *14* (7), 1404. https://doi.org/10.3390/v14071404.

(14) Narayanan, A.; Narwal, M.; Majowicz, S. A.; Varricchio, C.; Toner, S. A.; Ballatore, C.; Brancale, A.; Murakami, K. S.; Jose, J. Identification of SARS-CoV-2 Inhibitors Targeting Mpro and PLpro Using in-Cell-Protease Assay. *Commun Biol* **2022**, *5* (1), 1–17. https://doi.org/10.1038/s42003-022-03090-9.

(15) Protić, S.; Kaličanin, N.; Sencanski, M.; Prodanović, O.; Milicevic, J.; Perovic, V.; Paessler, S.; Prodanović, R.; Glisic, S. In Silico and In Vitro Inhibition of SARS-CoV-2 PLpro with Gramicidin D. *International Journal of Molecular Sciences* **2023**, *24* (3), 1955. https://doi.org/10.3390/ijms24031955.

(16) Lewis, D. S. M.; Ho, J.; Wills, S.; Kawall, A.; Sharma, A.; Chavada, K.; Ebert, M. C. C. J. C.; Evoli, S.; Singh, A.; Rayalam, S.; Mody, V.; Taval, S. Aloin Isoforms (A and B) Selectively Inhibits Proteolytic and Deubiquitinating Activity of Papain like Protease (PLpro) of SARS-CoV-2 in Vitro. *Sci Rep* **2022**, *12* (1), 2145. https://doi.org/10.1038/s41598-022-06104-y.

(17) Kulandaisamy, R.; Kushwaha, T.; Dalal, A.; Kumar, V.; Singh, D.; Baswal, K.; Sharma, P.; Praneeth, K.; Jorwal, P.; Kayampeta, S. R.; Sharma, T.; Maddur, S.; Kumar, M.; Kumar, S.; Polamarasetty, A.; Singh, A.; Sehgal, D.; Gholap, S. L.; Appaiahgari, M. B.; Katika, M. R.; Inampudi, K. K. Repurposing of FDA Approved Drugs Against SARS-CoV-2 Papain-Like Protease: Computational, Biochemical, and in Vitro Studies. *Front Microbiol* **2022**, *13*, 877813. https://doi.org/10.3389/fmicb.2022.877813.

(18) Loffredo, M.; Lucero, H.; Chen, D.-Y.; O'Connell, A.; Bergqvist, S.; Munawar, A.; Bandara, A.; De Graef, S.; Weeks, S. D.; Douam, F.; Saeed, M.; Munawar, A. H. The In-Vitro Effect of Famotidine on SARS-CoV-2 Proteases and Virus Replication. *Sci Rep* **2021**, *11* (1), 5433. https://doi.org/10.1038/s41598-021-84782-w.

(19) Klemm, T.; Ebert, G.; Calleja, D. J.; Allison, C. C.; Richardson, L. W.; Bernardini, J. P.; Lu, B. G.; Kuchel, N. W.; Grohmann, C.; Shibata, Y.; Gan, Z. Y.; Cooney, J. P.; Doerflinger, M.; Au, A. E.; Blackmore, T. R.; van der Heden van Noort, G. J.; Geurink, P. P.; Ovaa, H.; Newman, J.; Riboldi-Tunnicliffe, A.; Czabotar, P. E.; Mitchell, J. P.; Feltham, R.; Lechtenberg, B. C.; Lowes, K. N.; Dewson, G.; Pellegrini, M.; Lessene, G.; Komander, D. Mechanism and Inhibition of the Papain-like Protease, PLpro, of SARS-CoV-2. *The EMBO Journal* **2020**, *39* (18), e106275. https://doi.org/10.15252/embj.2020106275.

(20) Cho, H.; Kim, Y. J.; Chae, J.-W.; Meyer, M. R.; Kim, S. K.; Ryu, C. S. In Vitro Metabolic Characterization of the SARS-CoV-2 Papain-like Protease Inhibitors GRL0617 and HY-17542. *Frontiers in Pharmacology* **2023**, *14*.

(21) Cho, C.-C.; Li, S. G.; Lalonde, T. J.; Yang, K. S.; Yu, G.; Qiao, Y.; Xu, S.; Ray Liu, W. Drug Repurposing for the SARS-CoV-2 Papain-Like Protease. *ChemMedChem* **2022**, *17* (1), e202100455. https://doi.org/10.1002/cmdc.202100455.

(22) Ma, C.; Hu, Y.; Townsend, J. A.; Lagarias, P. I.; Marty, M. T.; Kolocouris, A.; Wang, J. Ebselen, Disulfiram, Carmofur, PX-12, Tideglusib, and Shikonin Are Nonspecific Promiscuous SARS-CoV-2 Main Protease Inhibitors. *ACS Pharmacol. Transl. Sci.* **2020**, *3* (6), 1265–1277. https://doi.org/10.1021/acsptsci.0c00130.

(23) Freitas, B. T.; Durie, I. A.; Murray, J.; Longo, J. E.; Miller, H. C.; Crich, D.; Hogan, R. J.; Tripp, R. A.; Pegan, S. D. Characterization and Noncovalent Inhibition of the Deubiquitinase and deISGylase Activity of SARS-CoV-2 Papain-Like Protease. *ACS Infect. Dis.* **2020**, *6* (8), 2099–2109. https://doi.org/10.1021/acsinfecdis.0c00168.

(24) Zhao, Y.; Du, X.; Duan, Y.; Pan, X.; Sun, Y.; You, T.; Han, L.; Jin, Z.; Shang, W.; Yu, J.; Guo, H.; Liu, Q.; Wu, Y.; Peng, C.; Wang, J.; Zhu, C.; Yang, X.; Yang, K.; Lei, Y.; Guddat, L. W.; Xu, W.; Xiao, G.; Sun, L.; Zhang, L.; Rao, Z.; Yang, H. High-Throughput Screening Identifies Established Drugs as SARS-CoV-2 PLpro Inhibitors. *Protein Cell* **2021**, *12* (11), 877–888. https://doi.org/10.1007/s13238-021-00836-9.

(25) Armstrong, L. A.; Lange, S. M.; Cesare, V. D.; Matthews, S. P.; Nirujogi, R. S.; Cole, I.; Hope, A.; Cunningham, F.; Toth, R.; Mukherjee, R.; Bojkova, D.; Gruber, F.; Gray, D.; Wyatt, P. G.; Cinatl, J.; Dikic, I.; Davies, P.; Kulathu, Y. Biochemical Characterization of Protease Activity of Nsp3 from SARS-CoV-2 and Its Inhibition by Nanobodies. *PLOS ONE* **2021**, *16* (7), e0253364. https://doi.org/10.1371/journal.pone.0253364.

(26) Maiti, B. K. Can Papain-like Protease Inhibitors Halt SARS-CoV-2 Replication? *ACS Pharmacol. Transl. Sci.* **2020**, *3* (5), 1017–1019. https://doi.org/10.1021/acsptsci.0c00093.

(27) Sargsyan, K.; Lin, C.-C.; Chen, T.; Grauffel, C.; Chen, Y.-P.; Yang, W.-Z.; S. Yuan, H.; Lim, C. Multi-Targeting of Functional Cysteines in Multiple Conserved SARS-CoV-2 Domains by Clinically Safe Zn-Ejectors. *Chemical Science* **2020**, *11* (36), 9904–9909. https://doi.org/10.1039/D0SC02646H.

(28) Lima, N. M.; Fernandes, B. L. M.; Alves, G. F.; de Souza, J. C. Q.; Siqueira, M. M.; Patrícia do Nascimento, M.; Moreira, O. B. O.; Sussulini, A.; de Oliveira, M. A. L. Mass Spectrometry Applied to Diagnosis, Prognosis, and Therapeutic Targets Identification for the Novel Coronavirus SARS-CoV-2: A Review. *Analytica Chimica Acta* **2022**, *1195*, 339385. https://doi.org/10.1016/j.aca.2021.339385.

(29) Yu, W.; Zhao, Y.; Ye, H.; Wu, N.; Liao, Y.; Chen, N.; Li, Z.; Wan, N.; Hao, H.; Yan, H.; Xiao, Y.; Lai, M. Structure-Based Design of a Dual-Targeted Covalent Inhibitor Against Papain-like and Main Proteases of SARS-CoV-2. *J. Med. Chem.* **2022**, *65* (24), 16252–16267. https://doi.org/10.1021/acs.jmedchem.2c00954.

(30) Wydorski, P. M.; Osipiuk, J.; Lanham, B. T.; Tesar, C.; Endres, M.; Engle, E.; Jedrzejczak, R.; Mullapudi, V.; Michalska, K.; Fidelis, K.; Fushman, D.; Joachimiak, A.; Joachimiak, L. A. Dual Domain Recognition Determines SARS-CoV-2 PLpro Selectivity for Human ISG15 and K48-Linked Di-Ubiquitin. *Nat Commun* **2023**, *14* (1), 2366. https://doi.org/10.1038/s41467-023-38031-5.

(31) Wu, D.; Robinson, C. V. Native Top-Down Mass Spectrometry Reveals a Role for Interfacial Glycans on Therapeutic Cytokine and Hormone Assemblies. *Angewandte Chemie International Edition n/a* (n/a). https://doi.org/10.1002/anie.202213170.

(32) Wang, H.; Eschweiler, J.; Cui, W.; Zhang, H.; Frieden, C.; Ruotolo, B. T.; Gross, M. L. Native Mass Spectrometry, Ion Mobility, Electron-Capture Dissociation, and Modeling Provide Structural Information for Gas-Phase Apolipoprotein E Oligomers. *J. Am. Soc. Mass Spectrom.* **2019**, *30* (5), 876–885. https://doi.org/10.1007/s13361-019-02148-z.

(33) Gadkari, V. V.; Ramírez, C. R.; Vallejo, D. D.; Kurulugama, R. T.; Fjeldsted, J. C.; Ruotolo, B. T. Enhanced Collision Induced Unfolding and Electron Capture Dissociation of Native-like Protein Ions. *Anal. Chem.* **2020**, *92* (23), 15489–15496. https://doi.org/10.1021/acs.analchem.0c03372.

(34) Lantz, C.; Lopez, J.; Goring, A. K.; Zenaidee, M. A.; Biggs, K.; Whitelegge, J. P.; Ogorzalek Loo, R. R.; Klärner, F.-G.; Schrader, T.; Bitan, G.; Loo, J. A. Characterization of Molecular Tweezer Binding on α-Synuclein with Native Top-Down Mass Spectrometry and Ion Mobility-Mass Spectrometry Reveals a Mechanism for Aggregation Inhibition. *J. Am. Soc. Mass Spectrom.* **2023**, *34* (12), 2739–2747. https://doi.org/10.1021/jasms.3c00281.

(35) Cong, X.; Liu, Y.; Liu, W.; Liang, X.; Russell, D. H.; Laganowsky, A. Determining Membrane Protein–Lipid Binding Thermodynamics Using Native Mass Spectrometry. *J. Am. Chem. Soc.* **2016**, *138* (13), 4346–4349. https://doi.org/10.1021/jacs.6b01771.

(36) Walker, T. E.; Shirzadeh, M.; Sun, H. M.; McCabe, J. W.; Roth, A.; Moghadamchargari, Z.; Clemmer, D. E.; Laganowsky, A.; Rye, H.; Russell, D. H. Temperature Regulates Stability, Ligand Binding (Mg2+ and ATP), and Stoichiometry of GroEL–GroES Complexes. *J. Am. Chem. Soc.* **2022**, *144* (6), 2667–2678. https://doi.org/10.1021/jacs.1c11341.

(37) McCabe, J. W.; Shirzadeh, M.; Walker, T. E.; Lin, C.-W.; Jones, B. J.; Wysocki, V. H.; Barondeau, D. P.; Clemmer, D. E.; Laganowsky, A.; Russell, D. H. Variable-Temperature Electrospray Ionization for Temperature-Dependent Folding/Refolding Reactions of Proteins and Ligand Binding. *Anal. Chem.* **2021**, *93* (18), 6924–6931. https://doi.org/10.1021/acs.analchem.1c00870.

(38) Rachel Mehaffey, M.; Ahn, Y.-C.; D. Rivera, D.; W. Thomas, P.; Cheng, Z.; W. Crowder, M.; F. Pratt, R.; Fast, W.; S. Brodbelt, J. Elusive Structural Changes of New Delhi Metallo-β-Lactamase Revealed by Ultraviolet Photodissociation Mass Spectrometry. *Chemical Science* **2020**, *11* (33), 8999–9010. https://doi.org/10.1039/D0SC02503H.

(39) Butalewicz, J.; Sipe, S.; Juetten, K.; James, V.; Meek, T.; Brodbelt, J. Insights into the Main Protease of SARS-CoV-2: Thermodynamic Analysis, Structural Characterization, and the Impact of Inhibitors. ChemRxiv November 6, 2023. https://doi.org/10.26434/chemrxiv-2023-lgv9f.

(40) O'Brien, J. P.; Li, W.; Zhang, Y.; Brodbelt, J. S. Characterization of Native Protein Complexes Using Ultraviolet Photodissociation Mass Spectrometry. *J. Am. Chem. Soc.* **2014**, *136* (37),

12920–12928. https://doi.org/10.1021/ja505217w.
(41) Sipe, S. N.; Lancaster, E. B.; Butalewicz, J. P.; Whitman, C. P.; Brodbelt, J. S. Symmetry of 4-Oxalocrotonate Tautomerase Trimers Influences Unfolding and Fragmentation in the Gas Phase. *J. Am. Chem. Soc.* **2022**, *144* (27), 12299–12309. https://doi.org/10.1021/jacs.2c03564.
(42) Osipiuk, J.; Azizi, S.-A.; Dvorkin, S.; Endres, M.; Jedrzejczak, R.; Jones, K. A.; Kang, S.; Kathayat, R. S.; Kim, Y.; Lisnyak, V. G.; Maki, S. L.; Nicolaescu, V.; Taylor, C. A.; Tesar, C.; Zhang, Y.-A.; Zhou, Z.; Randall, G.; Michalska, K.; Snyder, S. A.; Dickinson, B. C.; Joachimiak, A. Structure of Papain-like Protease from SARS-CoV-2 and Its Complexes with Non-Covalent Inhibitors. *Nat Commun* **2021**, *12* (1), 743. https://doi.org/10.1038/s41467-021-21060-3.
(43) Sacco, M. D.; Ma, C.; Lagarias, P.; Gao, A.; Townsend, J. A.; Meng, X.; Dube, P.; Zhang, X.; Hu, Y.; Kitamura, N.; Hurst, B.; Tarbet, B.; Marty, M. T.; Kolocouris, A.; Xiang, Y.; Chen, Y.; Wang, J. Structure and Inhibition of the SARS-CoV-2 Main Protease Reveal Strategy for Developing Dual Inhibitors against Mpro and Cathepsin L. *Science Advances* **2020**, *6* (50), eabe0751. https://doi.org/10.1126/sciadv.abe0751.
(44) Ma, C.; Sacco, M. D.; Hurst, B.; Townsend, J. A.; Hu, Y.; Szeto, T.; Zhang, X.; Tarbet, B.; Marty, M. T.; Chen, Y.; Wang, J. Boceprevir, GC-376, and Calpain Inhibitors II, XII Inhibit SARS-CoV-2 Viral Replication by Targeting the Viral Main Protease. *Cell Res* **2020**, *30* (8), 678–692. https://doi.org/10.1038/s41422-020-0356-z.
(45) El-Baba, T. J.; Lutomski, C. A.; Kantsadi, A. L.; Malla, T. R.; John, T.; Mikhailov, V.; Bolla, J. R.; Schofield, C. J.; Zitzmann, N.; Vakonakis, I.; Robinson, C. V. Allosteric Inhibition of the SARS-CoV-2 Main Protease: Insights from Mass Spectrometry Based Assays**. *Angewandte Chemie International Edition* **2020**, *59* (52), 23544–23548. https://doi.org/10.1002/anie.202010316.
(46) Sanders, J. D.; Shields, S. W.; Escobar, E. E.; Lanzillotti, M. B.; Butalewicz, J. P.; James, V. K.; Blevins, M. S.; Sipe, S. N.; Brodbelt, J. S. Enhanced Ion Mobility Separation and Characterization of Isomeric Phosphatidylcholines Using Absorption Mode Fourier Transform Multiplexing and Ultraviolet Photodissociation Mass Spectrometry. *Anal. Chem.* **2022**, *94* (10), 4252–4259. https://doi.org/10.1021/acs.analchem.1c04711.
(47) Blevins, M. S.; Juetten, K. J.; James, V. K.; Butalewicz, J. P.; Escobar, E. E.; Lanzillotti, M. B.; Sanders, J. D.; Fort, K. L.; Brodbelt, J. S. Nanohydrophobic Interaction Chromatography Coupled to Ultraviolet Photodissociation Mass Spectrometry for the Analysis of Intact Proteins in Low Charge States. *J. Proteome Res.* **2022**, *21* (10), 2493–2503. https://doi.org/10.1021/acs.jproteome.2c00450.
(48) Escobar, E. E.; Wang, S.; Goswami, R.; Lanzillotti, M. B.; Li, L.; McLellan, J. S.; Brodbelt, J. S. Analysis of Viral Spike Protein N-Glycosylation Using Ultraviolet Photodissociation Mass Spectrometry. *Anal. Chem.* **2022**, *94* (15), 5776–5784. https://doi.org/10.1021/acs.analchem.1c04874.
(49) Juetten, K. J.; Brodbelt, J. S. MS-TAFI: A Tool for the Analysis of Fragment Ions Generated from Intact Proteins. *J. Proteome Res.* **2023**, *22* (2), 546–550. https://doi.org/10.1021/acs.jproteome.2c00594.
(50) Shin, D.; Mukherjee, R.; Grewe, D.; Bojkova, D.; Baek, K.; Bhattacharya, A.; Schulz, L.; Widera, M.; Mehdipour, A. R.; Tascher, G.; Geurink, P. P.; Wilhelm, A.; van der Heden van Noort, G. J.; Ovaa, H.; Müller, S.; Knobeloch, K.-P.; Rajalingam, K.; Schulman, B. A.; Cinatl, J.; Hummer, G.; Ciesek, S.; Dikic, I. Papain-like Protease Regulates SARS-CoV-2 Viral Spread and Innate Immunity. *Nature* **2020**, *587* (7835), 657–662. https://doi.org/10.1038/s41586-020-2601-5.
(51) Jiang, H.; Yang, P.; Zhang, J. Potential Inhibitors Targeting Papain-Like Protease of SARS-CoV-2: Two Birds With One Stone. *Frontiers in Chemistry* **2022**, *10*.
(52) Mellott, D. M.; Tseng, C.-T.; Drelich, A.; Fajtová, P.; Chenna, B. C.; Kostomiris, D. H.; Hsu, J.; Zhu, J.; Taylor, Z. W.; Kocurek, K. I.; Tat, V.; Katzfuss, A.; Li, L.; Giardini, M. A.; Skinner, D.; Hirata, K.; Yoon, M. C.; Beck, S.; Carlin, A. F.; Clark, A. E.; Beretta, L.; Maneval, D.; Hook, V.; Frueh, F.; Hurst, B. L.; Wang, H.; Raushel, F. M.; O'Donoghue, A. J.; de Siqueira-Neto, J. L.; Meek, T. D.; McKerrow, J. H. A Clinical-Stage Cysteine Protease Inhibitor Blocks SARS-CoV-2 Infection of Human and Monkey Cells. *ACS Chem. Biol.* **2021**, *16* (4), 642–650. https://doi.org/10.1021/acschembio.0c00875.
(53) Edwards, A. N.; Blue, A. J.; Conforti, J. M.; Cordes, M. S.; Trakselis, M. A.; Gallagher, E. S.

Gas-Phase Stability and Thermodynamics of Ligand-Bound, Binary Complexes of Chloramphenicol Acetyltransferase Reveal Negative Cooperativity. *Anal Bioanal Chem* **2023**, *415* (25), 6201–6212. https://doi.org/10.1007/s00216-023-04891-5.

(54) Kundlacz, T.; Schmidt, C. Deciphering Solution and Gas-Phase Interactions between Peptides and Lipids by Native Mass Spectrometry. *Anal. Chem.* **2023**, *95* (47), 17292–17299. https://doi.org/10.1021/acs.analchem.3c03428.

(55) Nowak, Ł.; Krajewski, W.; Dejnaka, E.; Małkiewicz, B.; Szydełko, T.; Pawlak, A. Ubiquitin-Specific Proteases as Potential Therapeutic Targets in Bladder Cancer—In Vitro Evaluation of Degrasyn and PR-619 Activity Using Human and Canine Models. *Biomedicines* **2023**, *11* (3), 759. https://doi.org/10.3390/biomedicines11030759.

(56) Lin, W.-C.; Chiu, Y.-L.; Kuo, K.-L.; Chow, P.-M.; Hsu, C.-H.; Liao, S.-M.; Dong, J.-R.; Chang, S.-C.; Liu, S.-H.; Liu, T.-J.; Hsu, F.-S.; Wang, K.-C.; Lin, Y.-C.; Chang, C.-C.; Huang, K.-Y. Anti-Tumor Effects of Deubiquitinating Enzyme Inhibitor PR-619 in Human Chondrosarcoma through Reduced Cell Proliferation and Endoplasmic Reticulum Stress-Related Apoptosis. *Am J Cancer Res* **2023**, *13* (7), 3055–3066.

(57) James, V. K.; Sanders, J. D.; Aizikov, K.; Fort, K. L.; Grinfeld, D.; Makarov, A.; Brodbelt, J. S. Expanding Orbitrap Collision Cross-Section Measurements to Native Protein Applications Through Kinetic Energy and Signal Decay Analysis. *Anal. Chem.* **2023**, *95* (19), 7656–7664. https://doi.org/10.1021/acs.analchem.3c00594.